AMERICAN SOCIETY FOR MICROBIOLOGY | Molecular and Cellular Biology®

RESEARCH ARTICLE

Impact of Nuclear *De Novo* NAD$^+$ Synthesis via Histone Dynamics on DNA Repair during Cellular Senescence To Prevent Tumorigenesis

Masae Ikura,[a] Kanji Furuya,[b] Tomonari Matsuda,[c] Tsuyoshi Ikura[a]

[a]Laboratory of Chromatin Regulatory Network, Department of Genome Biology, Radiation Biology Center, Graduate School of Biostudies, Kyoto University, Kyoto, Japan
[b]Laboratory of Genome Maintenance, Department of Genome Biology, Radiation Biology Center, Graduate School of Biostudies, Kyoto University, Kyoto, Japan
[c]Research Center for Environmental Quality Management, Kyoto University, Otsu, Shiga, Japan

Masae Ikura and Kanji Furuya contributed equally to this work. Author order was determined in order of increasing seniority.

ABSTRACT NAD$^+$ synthesis is a fundamental process in living cells. The effects of local metabolite production on chromatin influence the epigenetic status of chromatin in DNA metabolism. We have previously shown that K5 acetylation of H2AX by TIP60 is required for the ADP ribosylation activity of PARP-1, for histone H2AX exchange at DNA damage sites. However, the detailed molecular mechanism has remained unclear. Here, we identified *de novo* NAD synthetase 1 (NAD syn1) as a novel binding partner to H2AX. The enzymatic activity of NAD syn1 is crucial for the ADP ribosylation activity of PARP-1 for the H2AX dynamics at sites of DNA damage. Inhibition of the NAD synthetase activity in the cell nucleus decreased the overall cellular NAD$^+$ concentration, leading to cellular senescence. Accordingly, the acetylation-dependent H2AX dynamics and homologous recombination repair were suppressed, leading to increased tumorigenesis. Our findings have revealed the importance of *de novo* NAD$^+$ production in the cell nucleus for protection against the decreased DNA repair capacity caused by cellular senescence and thus against tumorigenesis.

KEYWORDS DNA damage, NAD synthetase 1, TIP60, acetylation, cellular senescence, histone H2AX, tumorigenesis

NAD$^+$ is a central metabolite that plays a pivotal role in energy metabolism by serving as a coenzyme (1, 2). It also acts as a degradation substrate for a diverse range of enzymes, such as poly(ADP-ribose) polymerases (PARPs) and sirtuins, which function in the DNA damage response and transcriptional events (1–3). Since the cellular NAD$^+$ levels reportedly decline with age in many tissues, including liver, skin, and brain, NAD$^+$ is considered to be a crucial aging metabolite that provides a common link between aging-related genome instability, metabolic decline, and associated diseases such as neurodegeneration and cancer (1, 3). Thus, understanding how NAD$^+$ plays such diverse biological roles will provide novel therapeutic targets for the prevention of these age-related pathologies.

A careful balance between NAD$^+$ production and degradation regulates cellular NAD$^+$ levels (1, 3, 4). There are two pathways for NAD$^+$ production in cells. Most NAD$^+$ in mammals is produced in the salvage pathway, where NAD$^+$ is resynthesized from nicotinamide (NAM), a by-product of NAD-consuming enzymes such as sirtuins and PARPs (1, 3). In the other pathway, *de novo* NAD$^+$ synthesis starts from tryptophan catabolism, and it accounts for a minor fraction of the cellular NAD$^+$ pool (1, 3). Several recent reports have shown that the *de novo* NAD$^+$ synthesis pathway is active in liver, neuronal, and immune cells. Although these reports emphasized the potential role of *de novo* NAD$^+$ synthesis in whole-body NAD$^+$ homeostasis for preventing carcinogenesis (5–9), the regulation of these *de novo* NAD$^+$ synthesis pathways is yet to be elucidated.

Address correspondence to Tsuyoshi Ikura, ikura.tsuyoshi.3m@kyoto-u.ac.jp.

The authors declare no conflict of interest.

Received 1 September 2022
Returned for modification 13 September 2022
Accepted 27 September 2022
Published 24 October 2022

It is important to note that NAD^+ is not evenly distributed in the cell. In mitochondria, the NAD^+ content is 250 μM, while the estimated nuclear NAD^+ levels are much lower, around 70 μM (3, 10). The existence of different forms of nicotinamide mononucleotide adenylyltransferase (NMNAT1-3) in each cellular compartment suggests that NAD^+ metabolism is regulated according to compartment-specific metabolic requirements (3). The compartmentalization of NAD^+ synthesis may also have another layer of complexity (1). Recent reports have suggested that the local supplies of metabolites, such as *S*-adenosylmethionine (SAM) and acetyl coenzyme A (acetyl-CoA), for chromatin regulators at transcription promoters/enhancers influence the epigenetic status of chromatin for transcriptional activation (11–14). In fact, in NAD^+ metabolism, NMNAT1 is reportedly recruited to target gene promoters, dependent on either SIRT1 or PARP-1, suggesting that NAD^+ metabolism is regulated at a subnuclear level during transcriptional regulation (13, 14). These insights may partly explain the complexity of the spatial regulation of NAD^+ signaling. How NAD^+ metabolism is regulated for preventing aging and aging-related diseases is the next issue to consider.

We previously reported that the rapid exchange of histone H2AX on chromatin at DNA damage sites is facilitated by H2AX Lys 5 acetylation (K5 Ac) by TIP60 (15, 16). PARP-1 is included within the H2AX complex after genome DNA damage stress, and the acetylation of H2AX is required for the NAD^+-dependent poly(ADP-ribosyl)ation (PARylation) activity of PARP-1, which facilitates the dynamic binding of PARP-1 to chromatin at DNA damage sites (12). Since the PARP-1 activity is required to facilitate H2AX exchange, we proposed that H2AX and PARP-1 have reciprocal regulation of their dynamics on damaged chromatin; however, the mechanism underlying this regulation and its outcome is still unclear (12).

In this study, we identified NAD syn1, which is responsible for the *de novo* synthesis of NAD^+, as a component of the H2AX complex. We found that NAD syn1 is recruited onto DNA damage sites in an H2AX acetylation-dependent manner. This result suggested the possible role of *de novo* NAD^+ synthesis in nuclear chromatin. Therefore, we developed a system to specifically inhibit the *de novo* synthesis of NAD^+ only in the nucleus. This inhibition reduced the ADP-ribosylation activity of PARP-1 and its dynamic binding to DNA damage sites, which in turn inhibited the acetylation-dependent H2AX dynamics. Thus, the H2AX K5 Ac-dependent accumulation of NAD syn1 on damaged chromatin is crucial for PARP-1 activation, thus establishing that nuclear *de novo* NAD^+ synthesis is the crucial event for the reciprocal regulation between H2AX and PARP-1. Interestingly, the inhibition of nuclear *de novo* NAD^+ synthesis reduced the total levels of NAD^+ in the cell and mitochondrial energy metabolism, leading to premature cellular senescence. Defective homologous recombination repair at DNA double-stranded breaks (DSBs) was observed during the cellular senescence induced by the inhibition of the nuclear *de novo* NAD^+ synthesis, which coincided with an enhanced anchorage-independent proliferation of cancer cells. Collectively, for the first time, we show that the nuclear *de novo* NAD synthesis is regulated by chromatin dynamics, and our results explain the underlying mechanism to suppress the age-dependent decline in DNA repair capacity, which potentially leads to age-related pathology.

RESULTS

NAD syn1 is included in the H2AX complex and localized at DNA damage sites. We previously showed that H2AX is acetylated on lysine 5 (K5), and this acetylation is required for the NAD^+-dependent poly(ADP-ribosyl)ation (PARylation) activity of PARP-1 at the sites of DNA damage (12, 15). To investigate this mechanism, we performed a protein complex analysis of H2AX after DNA damage stress. From a series of mass spectrometry analyses on the protein complex of histone H2AX and its regulatory complexes (17), we identified NAD syn1 (NAD synthetase 1) as a candidate component of the H2AX complex. To confirm this, we performed an immunoblotting analysis of the H2AX complex before and after DNA damage. This complex was purified from nuclear extracts of HeLa cells stably expressing a C-terminally FLAG-hemagglutinin (HA)

epitope-tagged H2AX (eH2AX), by affinity chromatography on anti-FLAG antibody-conjugated agarose. The eH2AX complex bound to the agarose was eluted with the FLAG peptide under native conditions (15, 17). As a result, we confirmed the presence of NAD syn1 by an immunoblotting analysis using an anti-NAD syn1 antibody (Fig. 1A, "Input" lanes). The subsequent immunoprecipitation of the purified eH2AX complex with antibodies against NAD syn1 efficiently recovered eH2AX and NAD syn1 (Fig. 1A, "reciprocal IP" lanes). These reciprocal immunoprecipitation assays verified that NAD syn1 is a genuine component of the H2AX complex. Since NAD syn1 is the enzyme responsible for *de novo* NAD^+ production, these results suggest that NAD syn1 may be responsible for the H2AX acetylation-dependent PARylation activity of PARP-1.

De novo NAD^+ synthesis follows a glutamine-dependent pathway and is reportedly active in the liver (18). In this study, we compared glutamine dependency between the hepatocarcinoma cell line HepG2 and HeLa cells. To do so, we measured the degree of glutamine consumption during the response to DNA damage (2 Gy) in these two cell lines. We found a significant decrease of glutamine level in HepG2 cells compared to HeLa cells (see Fig. S1A in the supplemental material, data from 60 min after the irradiation [IR]), reflecting a higher degree of glutamine consumption upon the DNA damage response (2 Gy) in HepG2 cells. These results suggested that the higher glutamine metabolism activity, including glutamine-dependent *de novo* NAD^+ synthesis, occurs during the DNA damage response in HepG2 cells (19). Therefore, HepG2 is more suitable for analyses of the nuclear *de novo* NAD^+ synthesis than a cell line such as HeLa.

Various metabolic enzymes are recruited to transcriptional enhancers and promoters and may locally supply metabolites for epigenetic regulators (11, 13, 14, 20). To investigate whether NAD syn1 contributes to the acetylation-dependent PARylation activity of PARP-1, we explored the possibility that NAD syn1 may localize to sites of DNA damage in a manner dependent on the K5 acetylation of H2AX. Therefore, after confirming that H2AX K5 Ac was dependent on acetyltransferase TIP60 in HepG2 cells (Fig. 1B), as we reported for other cell lines, we performed a chromatin immunoprecipitation (ChIP) analysis using an anti-NAD syn1 antibody in HepG2 cells stably expressing either wild-type H2AX (H2AX-WT) or a mutant H2AX in which Lys 5 is replaced with arginine (H2AX K5R), under the control of the CAG promoter, after transfection with the H2AX small interfering RNA (siRNA), which targets a noncoding region (Fig. 1C). These HepG2 cells were then transfected with Cas9/single guide RNA (sgRNA), to introduce a DNA DSB at a specific site in the adeno-associated virus integration site (AAVS) locus. The subsequent quantitative PCR (qPCR) analysis revealed that the amount of NAD syn1 significantly increased, especially at a site 600 bp away from the DSB, in the H2AX-WT-expressing HepG2 cells, indicating the NAD syn1 accumulation at the damaged chromatin (Fig. 1C; Fig. S1B). In contrast, in the HepG2 cells stably expressing H2AX-K5R, NAD syn1 was not significantly accumulated at the site 600 bp away from the DSB, compared to that in the cells expressing H2AX-WT (Fig. 1C). To confirm the acetylation-dependent accumulation of NAD syn1 on damaged chromatin after DSB induction, we performed a ChIP analysis using cells stably expressing the siRNA-resistant TIP60 or TIPM (TIP60 acetyltransferase activity deficient) under the control of the CAG promoter and transiently expressing the TIP60 siRNA (Fig. 1D). We found significant accumulation of NAD syn1 at the site 600 bp away from the DSB in the TIP60-expressing cells, compared to the TIPM-expressing cells (Fig. 1D; Fig. S1B). These results indicated that TIP60-dependent acetylation is responsible for the recruitment of NAD syn1 to the sites of DNA damage. It should be noted that we and others have shown that TIP60 is involved in homologous recombination (HR) repair (15, 21). During HR repair, the DSB end is resected, and it has been reported that HR protein RAD51 binds not at the DNA end-proximal region but at a site away from the DSB in ChIP analysis (22). Therefore, our results showing that the accumulation of NAD syn1 was found not 180 bp but rather 600 bp away from the DSB site suggest the possible involvement of NAD syn1 in HR repair.

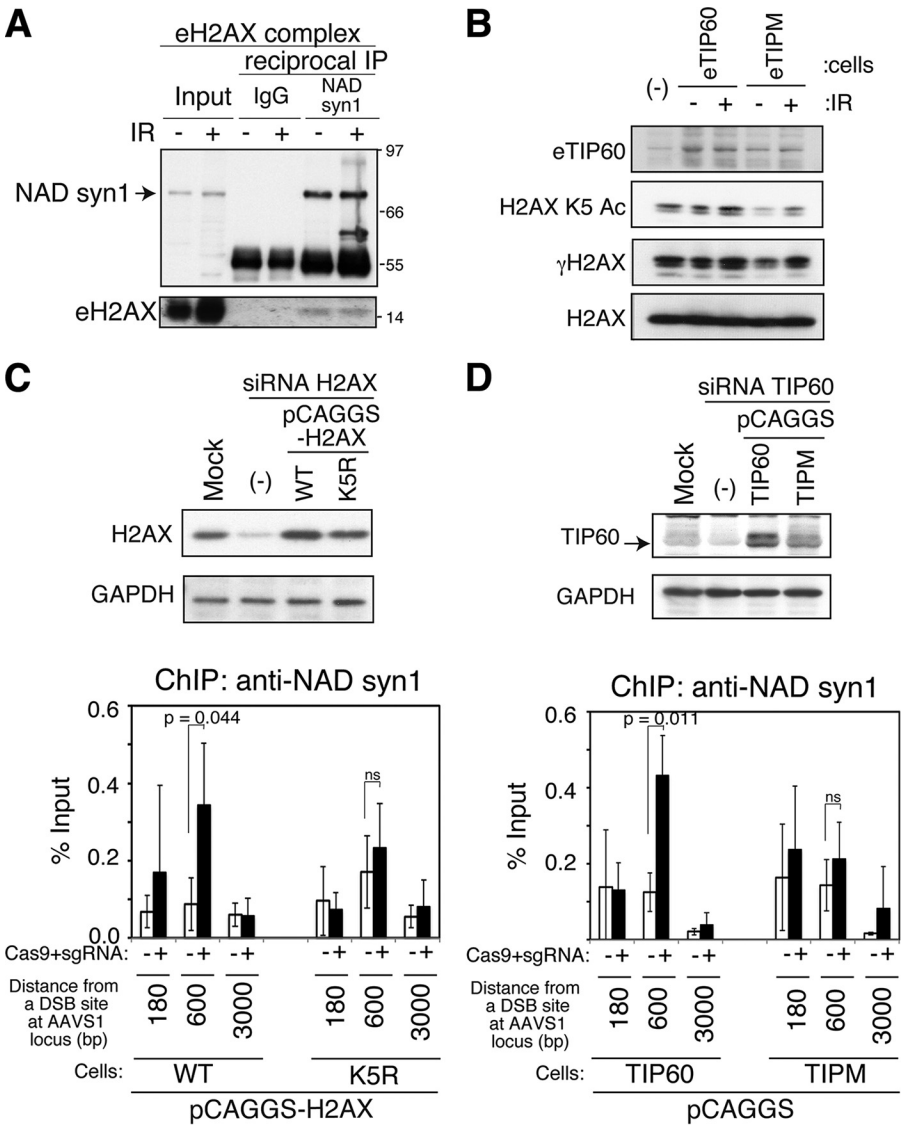

FIG 1 NAD synthetase 1 (NAD syn1) is included in the H2AX complex in a manner dependent on H2AX K5 Ac for recruitment to the sites of DNA damage. (A) The eH2AX complexes were immunoaffinity purified from the nuclear soluble fraction of HeLa cells treated without (−) or with (+) 3 Gy gamma irradiation (IR), followed by a 5-min recovery. The immunopurified eH2AX complex was subsequently immunoprecipitated (reciprocal IP) by antibody against NAD syn1 or by IgG control and was analyzed by immunoblotting against antibody against NAD syn1 or H2AX. (B) Immunoblot analysis of whole-cell extracts from the HepG2 cells stably expressing eTIP60 or eTIPM after SDS-PAGE. Anti-FLAG (eTIP60), anti-H2AX-K5 Ac, and anti-H2AX antibodies were used. IR: 3 Gy, followed by a 10-min recovery. (C) ChIP analysis by qPCR, for NAD syn1 accumulation at the defined DSB induced by Cas9 targeting AAVS1 locus in HepG2 cells stably expressing H2AX-WT or H2AX-K5R. (Top) Immunoblot analysis of whole-cell extracts from the HepG2 cells stably expressing H2AX-WT or -K5R after knockdown of endogenous H2AX. (Bottom) qPCR results of ChIP analysis. Error bars show standard deviations (SD) from three independent experiments. *P* values were determined by Student's *t* test. (D) ChIP analysis by qPCR, for NAD syn1 accumulation at the defined DSB induced by Cas9 targeting the AAVS1 locus in HepG2 cells stably expressing TIP60-WT or TIPM. (Top) Immunoblot analysis of whole-cell extracts from HepG2 cells stably expressing TIP60-WT or TIPM after knockdown of endogenous TIP60. (Bottom) qPCR results of ChIP analysis. Error bars show SD from three independent experiments. *P* values were determined by Student's *t* test.

Experimental system for expressing the NAD syn1 catalytic mutant to assess the impact of nuclear *de novo* NAD$^+$ synthesis activity on cellular functions. Our results suggested the significance of *de novo* NAD$^+$ synthesis in the nuclear compartment. However, most NAD$^+$ synthesis takes place in the cytoplasm (3). Therefore, to investigate the role of nuclear *de novo* NAD$^+$ synthesis, we took the approach of

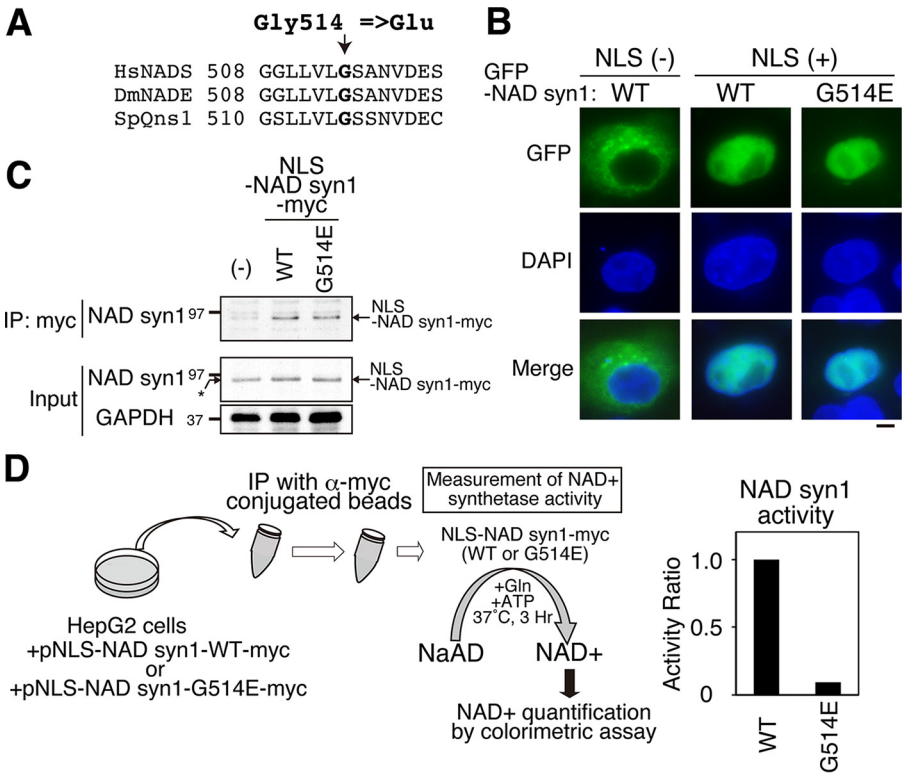

FIG 2 Experimental system to express the NAD syn1 catalytic mutant in the nucleus to inhibit nuclear *de novo* NAD synthesis. (A) Schematic representation of the region near Gly 514 of NAD syn1. A point mutation of G514E, which has been reported to lower catalytic activity 200-fold in other organisms, was introduced into NAD syn1. (B) GFP-NAD syn1-GFP, GFP-NLS-NAD syn1, and GFP-NLS-NAD syn1-G514E were expressed in HepG2 cells and subjected to fluorescence microscopy analysis. (C) NLS-NAD syn1-WT-myc (WT) and NLS-NAD syn1-G514E-myc (G514E) was expressed in HepG2 cells, and proteins were purified with an anti-myc antibody. Immunoblotting analyses were performed with anti-NAD syn1 and anti-GAPDH antibodies. The asterisk indicates endogenous NAD syn1 overlapping NLS-NAD syn1. (D) NAD^+ synthetase activity was measured with immunopurified NLS-NAD syn1-WT-myc (WT) or NLS-NAD syn1-G514E-myc (G514E) proteins. (Left) Schematic diagram of the experimental design to assess the NLS-NAD syn1 activity from cells. (Right) NAD syn1 activity plotted on a histogram (see Materials and Methods for details).

specifically inhibiting the endogenous nuclear NAD syn1 enzymatic activity by ectopically expressing a catalytically inactive mutant of NAD syn1 in the nucleus (23). To construct the expression system, we first introduced a glycine to glutamine substitution mutation at amino acid 514 (G514E) of the NAD syn1 gene on the plasmid. This G514E mutation reportedly results in defective glutamine-dependent NAD synthase activity (Fig. 2A) (24). The WT and G514E mutant genes of NAD syn1 were then fused with a nuclear localization signal (NLS) to force their expression in the nucleus (NLS-NAD syn1-WT or -G514E) (25). We confirmed that both the NLS-NAD syn1-WT and the G514E mutant are localized in the nucleus by constructing GFP-tagged NLS-NAD syn1-WT and -G514E, expressing them in HepG2 cells, and analyzing the cells by fluorescence microscopy (Fig. 2B).

We next sought to determine whether the expressed NLS-NAD syn1-G514E has reduced NAD synthetase activity compared to NLS-NAD syn1-WT in the nucleus. For this purpose, NLS-NAD syn1-WT and -G514E were C-terminally tagged with myc and expressed in HepG2 cells, and then NLS-NAD syn1-WT-myc and -G514E-myc were purified using anti-myc antibody-conjugated beads, followed by elution with myc peptides (Fig. 2C). The purified NLS-NAD syn1-WT-myc and -G514E-myc were subjected to an *in vitro* NAD synthetase activity assay (Fig. 2D) (26). As expected, the glutamine-dependent NAD synthetase activity was greatly inhibited with the purified NLS-NAD syn1-G514E-myc protein, compared to the NLS-NAD syn1-WT-myc protein (Fig. 2D). Thereby, we

established an experimental system for testing the effects of inhibiting nuclear *de novo* NAD synthesis on various cellular functions.

Nuclear *de novo* synthesis of NAD^+ is crucial for PARylation activity of PARP-1 and H2AX dynamics at DNA damage sites. We previously established a system in which the DNA damage-dependent PARylation activity of PARP-1 can be assessed, by quantifying the dynamic binding of PARP-1–GFP to chromatin through analysis using fluorescence recovery after photobleaching (FRAP) in combination with microirradiation (12). Since our previous work on PARP-1 dynamics was performed in a human fibroblast cell line, GM0637 (12), we first examined whether the PARP-1 dynamics also depends on its PARylation activity in HepG2 cells. We therefore established HepG2 cell lines that stably expressed siRNA-resistant wild-type PARP-1 tagged with green fluorescent protein (PARP-1–GFP) or the siRNA-resistant PARP-1–GFP derivative lacking catalytic activity (E988K) (Fig. S2A). These cells were transfected with the PARP-1 siRNA and subjected to a FRAP analysis in combination with microirradiation. After confirming that PARP-1–GFP WT and E988K were equally accumulated at the microirradiated area in each cell (Fig. S2B), the GFP signals at the microirradiated area were photobleached, and the fluorescence recovery was monitored (Fig. S2C). As expected, the fluorescence recovery of the PARP-1 E988K–GFP mutant after photobleaching was strongly inhibited, compared to that of the PARP-1–GFP wild type (Fig. S2C). This result was verified by calculating the mean residence time of PARP-1 GFPs in the microirradiated area, which was significantly longer in PARP-1 E988K–GFP than in wild-type PARP-1–GFP (27) (Fig. S2D; also, see Materials and Methods). Thus, we established an experimental system to assess the PARP-1 activity by PARP-1–GFP dynamics in HepG2 cells.

Having shown that K5-acetylated H2AX recruits NAD syn1 to sites of DNA damage (Fig. 1), we hypothesized that the NAD syn1 enzymatic activity might be necessary for the K5 acetylation-dependent PARylation activity of PARP-1 at damaged chromatin. To test this possibility, we examined whether the nuclear *de novo* NAD synthesis is required for PARP-1 dynamics on damaged chromatin. Therefore, we performed a FRAP analysis of PARP-1–GFP in combination with microirradiation, in HepG2 cells expressing NLS-NAD syn1-WT-myc or NLS-NAD syn1-G514E-myc (Fig. 2), in which PARP-1–GFP was also stably expressed ectopically (Fig. 3A). After confirming the equal accumulation of PARP-1–GFP in each cell within the microirradiated area (Fig. 3B and C), the GFP fluorescence was photobleached, and the fluorescence recovery of PARP-1–GFP was monitored. We found that the fluorescence recovery of PARP-1–GFP in cells expressing NLS-NAD syn1-G514E was greatly inhibited compared to that in cells expressing NLS-NAD syn1-WT (Fig. 3D). The loss of PARP-1 dynamics in NLS-NAD syn1-G514E-expressing HepG2 cells was verified by measuring the mean residence time (Fig. 3D). It should be noted that PARP-1 dynamics in cells expressing NLS-NAD syn1-WT was comparable to those in control HepG2 cells, excluding the possibility that NAD syn1 ectopic expression affects PARP-1 dynamics (Fig. 3D; Fig. S2D; compare the mean residence time of PARP-1 GFP in control HepG2 cells and NLS-NAD syn1-WT-expressing HepG2 cells). These results indicate that the nuclear *de novo* NAD^+ synthesis activity is required for the PARylation activity of PARP-1 at sites of DNA damage.

To confirm these results, since PARP-1 itself is known to become auto-PARylated upon DNA damage (28–30), we examined whether this activity is compromised in HepG2 cells expressing NLS-NAD syn1-G514E. We performed immunoprecipitations using an anti-PAR antibody with nuclear extracts from the HepG2 cell lines expressing NLS-GFP-NAD syn1-WT-myc and -G514E-myc, and then we analyzed the immunoprecipitated proteins by immunoblotting with anti-PARP-1. As expected, we observed significant reduction of the auto-PARylation of PARP-1 in NLS-GFP-NAD syn1-G514E-expressing cells compared to that in NLS-GFP-NAD syn1-WT-expressing cells (Fig. 3E). Taken together, these results indicate that nuclear *de novo* NAD^+ synthesis regulated by TIP60-dependent acetylation supplied NAD^+ at the site of DNA damage to promote a PARylation activity-dependent PARP-1 dynamics.

In our previous study, we showed that the PARylation activities of PARP-1 and H2AX K5 Ac by TIP60 are mutually regulated (12). This reciprocal regulation forms positive feedback regulation to facilitate H2AX exchange at sites of DNA damage for

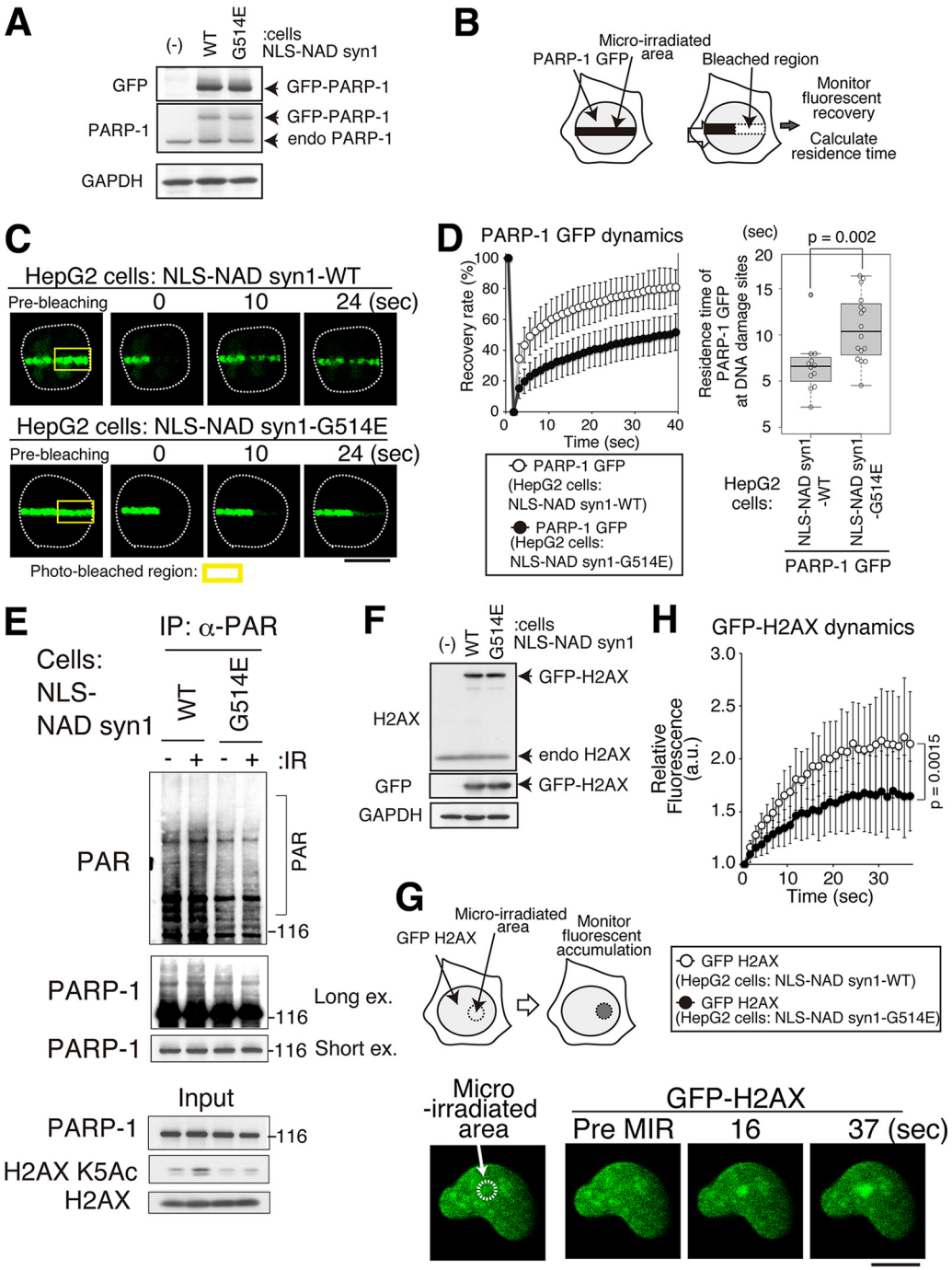

FIG 3 Inhibition of *de novo* synthesis of NAD^+ compromises PARylation activity of PARP-1 and H2AX dynamics at DNA damage sites. (A) PARP-1–GFP was stably and ectopically expressed in HepG2 cells expressing NLS-NAD syn1-WT-myc or NLS-NAD syn1-G514E-myc (the cell line established as shown in Fig. 2 was used). Immunoblotting analysis was performed with the indicated antibodies. (B) Schematic of FRAP analysis using PARP-1–GFP. (C) FRAP analysis to monitor the dynamics of PARP-1–GFP in HepG2 cells expressing NLS-NAD syn1-WT or -G514E. The PARP-1–GFP accumulated at the micr-oirradiated area was photobleached, and fluorescence recovery was monitored. Bar, 10 μm. (D) (Left) Quantification of the fluorescence recovery of PARP-1–GFP in panel C. (Right) Box plot showing mean residence time of the PARP-1–GFP microirradiated area in panel D. *P* values were determined with the Wilcoxon rank sum test. NLS-NAD syn1-WT; n = 12; NLS-NAD syn1-G514E, n = 16. (E) (Top) Anti-PAR antibody immunoprecipitates were subjected to an immunoblot analysis using anti-PARP-1 and anti-PAR antibodies. Unirradiated or 3-Gy-irradiated (followed by a 10-min recovery) HepG2 cells stably expressing NLS-NAD syn1-WT or G514E were used for immunoprecipitation. Long ex., long exposure to compare PARylated PARP-1 signals between NLS-NAD syn1-WT- and NLS-NAD syn1-G514E-expressing cells. Short ex., short exposure to show that the same amount of PARP-1 was immunoprecipitated with anti-PAR antibody. (Bottom) Input nuclear extracts immunoblotted with anti-PARP-1, anti-H2AX, and anti-H2AX K5 Ac antibodies. (F) Immunoblotting analysis of NLS-GFP-NAD syn1-WT-myc- or -G514E-myc-expressing cells overexpressing GFP-H2AX WT, using anti-GFP, anti-PARP-1, and anti-GAPDH

(Continued on next page)

homologous recombination (HR) repair (15, 16). To examine whether the nuclear *de novo* NAD^+ synthesis activity is required for H2AX K5 Ac, we performed an immunoblot analysis with anti-H2AX K5 Ac. Consistently, H2AX K5 Ac was decreased in NLS-GFP-NAD syn1-G514E-expressing cells compared to NLS-GFP-NAD syn1-WT-expressing cells (Fig. 3E). These results indicate that nuclear *de novo* NAD^+ synthesis and H2AX K5 Ac also undergo reciprocal regulation, which might be important for H2AX exchange at the site of DNA damage. We have already found that the role of K5 acetylation of H2AX is to promote the incorporation of H2AX into the DNA damage sites for H2AX exchange (M. Ikura, K. Furuya, and T. Ikura, submitted for publication). Therefore, we examined whether the nuclear *de novo* NAD^+ synthesis activity is required for H2AX assembly at sites of DNA damage, by monitoring the accumulation of GFP-tagged H2AX at DNA damage sites, using a confocal microscope equipped with a laser microirradiation system (Fig. 3G; also, see Materials and Methods). We overexpressed N-terminally GFP-tagged H2AX (GFP-H2AX WT) in the HepG2 cell lines stably expressing NLS-GFP-NAD syn1-WT-myc or -G514E-myc (Fig. 3F). Then, we monitored the accumulation of GFP-H2AX after the microirradiation of these HepG2 cells. Rapid accumulation of GFP-H2AX at the microirradiated area was observed in cells expressing NLS-NAD syn1-WT, while the accumulation was significantly reduced in cells expressing NLS-NAD syn1-G514E (Fig. 3H). Overall, these results indicate that nuclear *de novo* NAD^+ synthesis is necessary for the PARylation activity of PARP-1 for H2AX dynamics at the sites of DNA damage.

Nuclear *de novo* synthesis of NAD^+ is crucial for cellular NAD^+ homeostasis and mitochondrial energy metabolism to prevent premature cellular senescence. The results in Fig. 3 suggest that NAD syn1 can locally supply NAD^+ to PARP-1 for its PARylation activity at the site of DNA damage (Fig. 4A). However, we still could not rule out the possibility that NAD^+ might also originate from other compartments than the nucleus. Therefore, we examined the cellular NAD^+ levels in HepG2 cells expressing NLS-GFP-NAD syn1-WT and -G514E. The cell lysates were prepared from NLS-NAD syn1-WT- and -G514E-expressing cells after 2 Gy of irradiation. These cell lysates were subjected to a colorimetric assay to quantify the amounts of cellular NAD^+ and NADH (31) (see Materials and Methods). Intriguingly, we observed reduced amounts of NAD^+ and NADH in the NLS-NAD syn1-G514E-expressing cells compared to the NLS-NAD syn1-WT-expressing cells (Fig. 4B, panel i).

It should be noted that NAD syn1 exists in both the nucleus and cytosol. When *de novo* NAD^+ synthesis was inhibited in both the nucleus and cytosol, by expressing non-NLS-fused NAD^+ syn1 or by depleting NAD syn1 (knockdown of NAD syn1) (Fig. S3A), almost the same amounts of NAD^+ and NADH were detected between cells expressing non-NLS-fused NAD syn1-WT and -G514E (Fig. 4B, panel ii) or between mock-transfected cells and cells transfected with NAD syn1 siRNA (Fig. S3B). The sustained NAD^+ levels in NAD syn1 knockdown cells were also confirmed by showing that PARP-1–GFP and GFP-H2AX dynamics at the sites of DNA damage in NAD syn1 knockdown cells were comparable to those of control HepG2 cells (Fig. S3C and D). This is probably because the NAD^+ salvage pathway compensates for the absence of NAD syn1 activity in the cytoplasm (Fig. 4A), suggesting the importance of compartment-specific regulation of *de novo* NAD^+ synthesis. Therefore, these results indicate that our established system, which exerted a dominant negative effect to inhibit nuclear *de novo* NAD^+ synthesis activity, is useful for extracting the role of NAD syn1 in the nucleus and confirm the critical role of nuclear *de novo* NAD^+ synthesis in maintaining the whole-cell NAD^+ content. This whole-cell NAD^+ reduction might cause the decreased PARP-1 dynamics at damaged chromatin.

The maintenance of the mitochondrial NAD pool reportedly has critical importance for mitochondrial energy metabolism (32). Therefore, we investigated whether the

FIG 3 Legend (Continued)
antibodies. (G) (Top) Schematic of the microirradiation experiment to monitor H2AX dynamics. (Bottom) Example of GFP-H2AX accumulation at an microirradiated region in a cell nucleus. (H) The accumulation of GFP-H2AX at microirradiated area was quantified and compared between HepG2 cells expressing NLS-NAD syn1-WT and those expressing NLS-NAD syn1-G514E. *P* values were determined with Student's *t* test (NLS-NAD syn1-WT, $n = 13$; NLS-NAD syn1-G514E, $n = 16$).

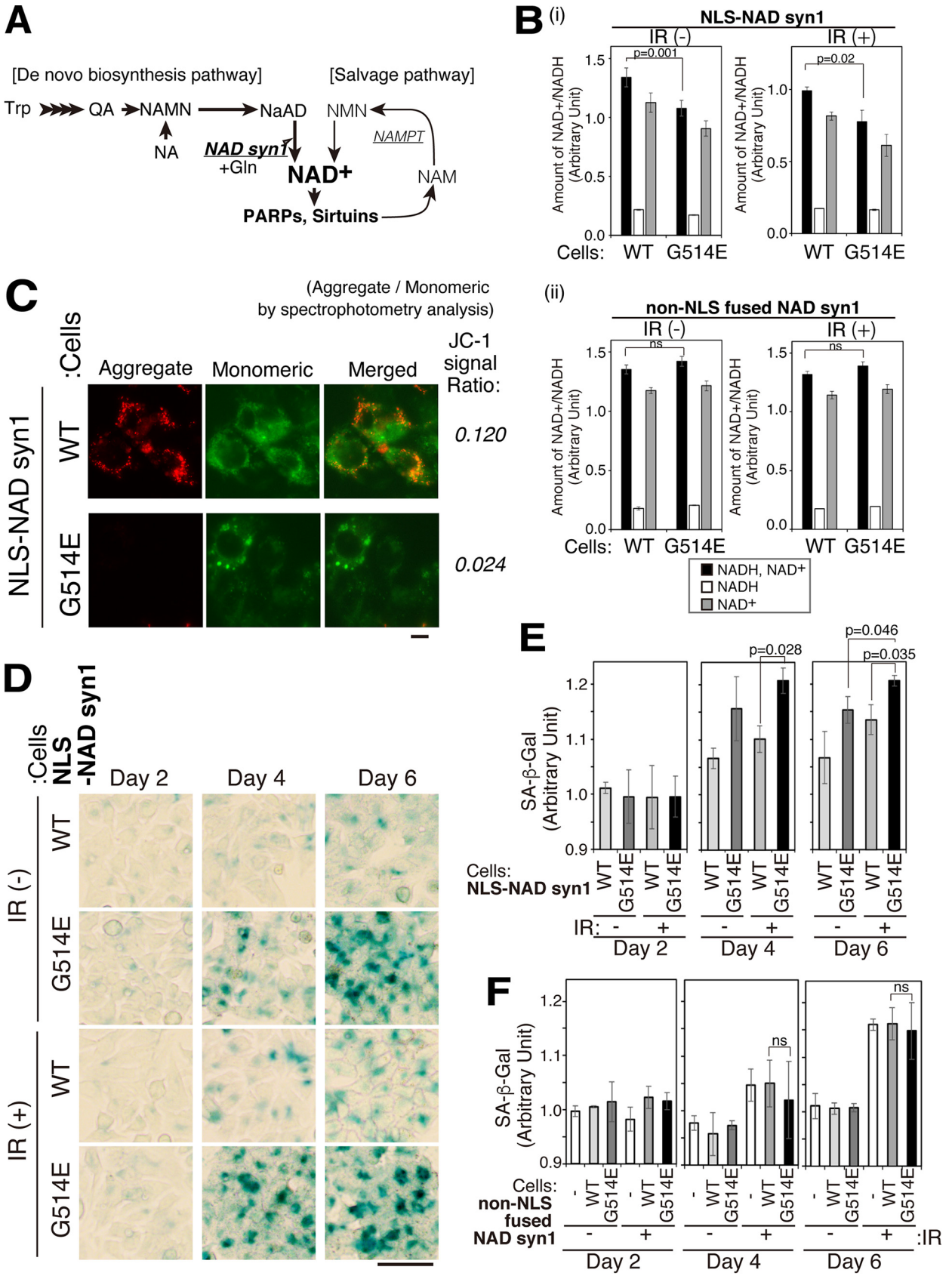

FIG 4 Inhibition of nuclear *de novo* synthesis of NAD^+ disrupts cellular NAD^+ homeostasis and mitochondrial energy metabolism, leading to premature cellular senescence. (A) Schematic diagram of NAD^+ metabolism in the cell. (B) Intracellular levels of NAD^+ and NADH levels were

(Continued on next page)

decreased NAD^+ and NADH pools, after the inhibition of nuclear *de novo* NAD^+ synthesis, affect the mitochondrial membrane potential, an indicator of mitochondrial energy metabolism. To do so, we compared the mitochondrial membrane potentials in HepG2 cells expressing NLS-NAD syn1-WT or -G514E by staining with a mitochondrial membrane potential indicator, JC-1 dye. The results revealed that, while NLS-NAD syn1-WT-expressing cells showed bright red JC-1 fluorescence, indicating the high membrane potential of mitochondria, the NLS-NAD syn1-G514E-expressing cells did not display the red fluorescence (Fig. 4C) (33). These findings indicate that the inhibition of nuclear *de novo* NAD^+ synthesis compromises the energy metabolism in mitochondria.

The loss of NAD^+ and the decreased mitochondrial membrane potential have been linked to cellular senescence (34). Therefore, to test whether the inhibition of nuclear *de novo* NAD^+ synthesis induces cellular senescence, we performed senescence-associated β-galactosidase (SA-β-Gal) staining of HepG2 cells expressing either NLS-NAD syn1-WT or -G514E or either non-NLS-fused NAD syn1-WT or -G514E or just HepG2 cells. As a result, the number of SA-β-Gal-stained HepG2 cells expressing NLS-NAD syn1-G514E was remarkably increased compared to that of the cells expressing NLS-NAD syn1-WT, non-NLS-fused NAD syn1-WT, or non-NLS-fused NAD syn1-G514E and of HepG2 cells alone, regardless of gamma irradiation (Fig. 4D to F; Fig. S4A and B). Altogether, these results indicate the crucial role of nuclear *de novo* NAD^+ synthesis in controlling whole-cell NAD^+ metabolism and mitochondrial energy metabolism to prevent premature cellular senescence.

Inhibition of nuclear *de novo* NAD^+ synthesis leads to impaired homologous recombination repair and enhances tumorigenesis. DNA repair capacity reportedly decreases with age, and this is thought to cause age-related pathologies, such as cancer (35). Thus, we investigated whether the DNA repair activity is affected when the inhibition of nuclear *de novo* NAD^+ synthesis induces premature cellular senescence. We focused on DNA DSBs, which are considered the most toxic lesion, as they potentially affect cell fate (36). The DSBs in cells are mainly repaired by one of the two major pathways: HR and nonhomologous-end joining (NHEJ), and we and others have shown that the acetylation of H2AX by TIP60 and PARP-1 facilitates HR repair while restricting NHEJ (16, 21, 37, 38). Therefore, we examined the HR efficiency in cells expressing NLS-GFP-NAD syn1-WT or -G514E by using the ASHRA (assay for site-specific HR activity) system, which allowed us to measure the HR repair efficiencies at a defined DSB in the β-actin gene (ACTB) region (Fig. 5A) (39). Reduced HR efficiency was observed in the cells expressing NLS-GFP-NAD syn1-G514E, compared to that in the cells expressing NLS-GFP-NAD syn1-WT (Fig. 5A). The defective HR repair in the HepG2 cells expressing NLS-GFP-NAD syn1-G514E was confirmed by an immunohistochemistry analysis, using an antibody against the HR protein RAD51. As expected, we found a reduced number of damage-induced RAD51 foci in the HepG2 cells expressing NLS-NAD syn1-G514E compared to that in the cells expressing NLS-NAD syn1-WT or non-NLS-fused NAD syn1-WT or -G514E (Fig. 5B; Fig. S5A). Together, these results indicate that HR failed to repair DSBs in cells where the nuclear *de novo* NAD^+ synthesis was inhibited.

HR repair is regarded as an accurate repair pathway, and its deficiencies lead to a predisposition to cancer development (40, 41). One of the hallmarks of aggressive cancer cells is the ability to grow under anchorage-independent conditions (42). Therefore, we examined whether the inhibition of *de novo* NAD^+ synthesis affects the growth of

FIG 4 Legend (Continued)
quantified in (i) NLS-NAD syn1-WT- or -G514E-expressing HepG2 cells or (ii) non-NLS-fused NAD syn1-WT- or -G514E-expressing HepG2 cells, with or without IR (followed by a 10-min recovery). For the determination of the concentration, see Materials and Methods. Error bars show SD ($n = 3$). (C) Mitochondria of HepG2 cells expressing NLS-NAD syn1-WT or -G514E were observed after incubation with JC-1. "Aggregate" corresponds to red (590-nm emission) signal of JC-1, indicating the high membrane potential of mitochondria, while "monomeric" corresponds to the green (535-nm emission) signal, indicating low membrane potential. The high aggregate/monomeric fluorescence ratio represents high mitochondrial energy metabolism (33). (D) HepG2 cells expressing NLS-NAD syn1-WT or -G514E were cultured after 2 Gy of IR and stained for SA-β-Gal. Days 2, 4, and 6 correspond to 2, 4, and 6 days after the IR. Bar, 250 μm. Gamma values for photo images were set as 1.5. (E and F) SA-β-Gal activity in HepG2 cells expressing NLS-NAD syn1-WT or -G514E (E) and HepG2 cells expressing non-NLS-fused NAD syn1-WT or -G514E (F) after 2 Gy of IR was quantified using a SPiDER-β-Gal kit (Dojindo). The SA-β-Gal activity is indicated as the ratio to the no-cell-control background. Error bars show SD. *P* values were determined with Student's *t* test for 3 technical replicates. See Materials and Methods for details.

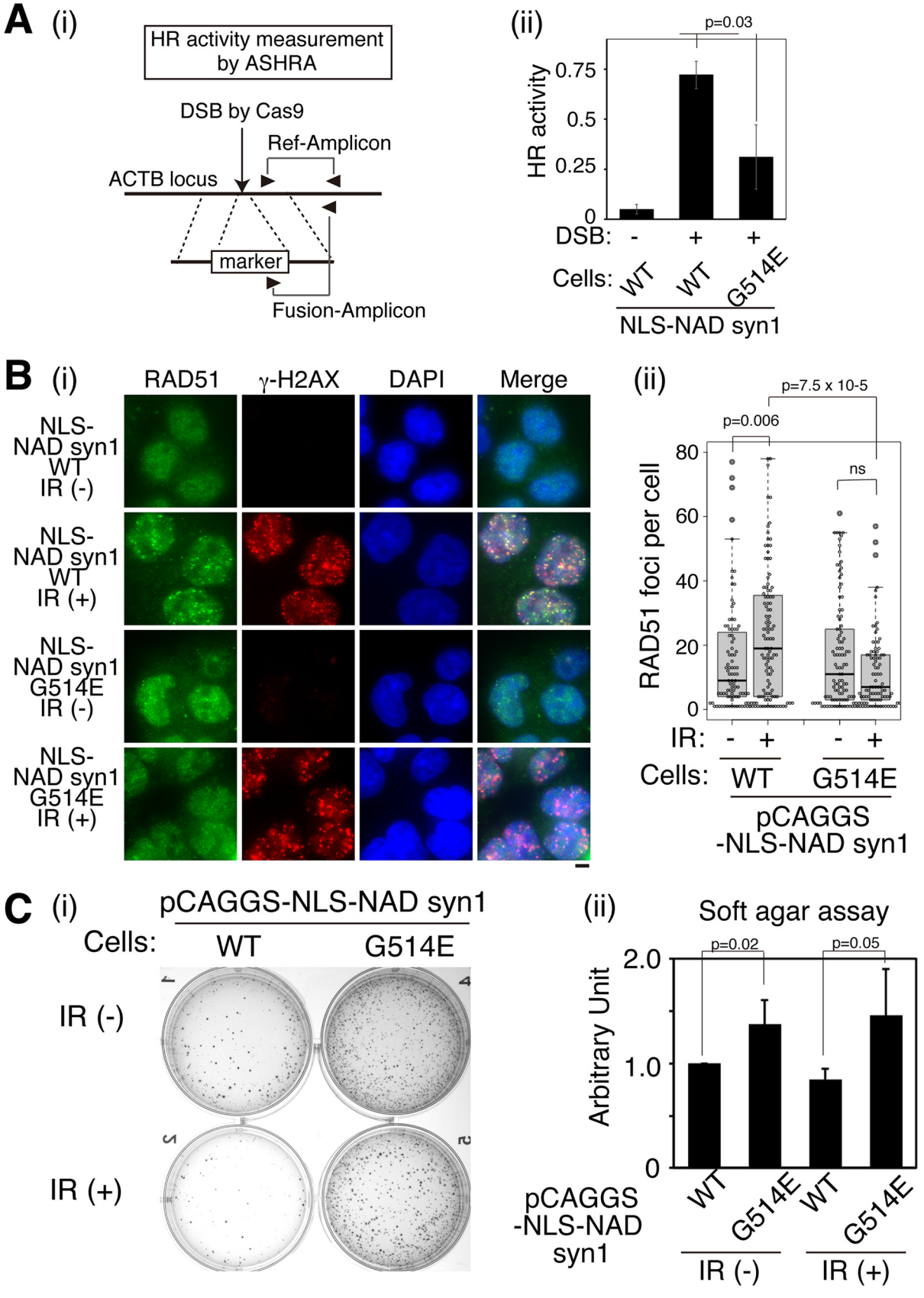

FIG 5 Inhibition of nuclear *de novo* NAD^+ synthesis leads to impaired homologous recombination repair and facilitates anchorage-independent cell growth. (A) (i) Schematic of ASHRA. (ii) HR efficiency was measured at a defined DSB (Cas9-ACTB sgRNA) using ASHRA in NLS-NAD

(Continued on next page)

HepG2 cells in soft agar. The colony numbers of cells expressing NLS-NAD syn1-G514E were significantly increased compared to those of the cells expressing NLS-NAD syn1-WT, both with and without irradiation (Fig. 5C). When we expressed non-NLS-fused NAD syn1-G514E in HepG2 cells, we did not observe increased colony number compared to just HepG2 or non-NLS-fused NAD syn1-WT expressing HepG2 cells (Fig. S5B). These suggest the significance of nuclear *de novo* NAD^+ synthesis in suppression of anchorage-independent cell growth. Together, these results indicate that increased genomic instability and accelerated tumorigenesis occur when cellular senescence is induced by the inhibition of nuclear *de novo* NAD^+ synthesis.

DISCUSSION

In this study, we demonstrated the crucial role of *de novo* NAD^+ synthesis in the nucleus for maintaining whole-cell NAD^+ homeostasis to suppress cellular senescence and tumorigenesis. To address this issue, we established a novel experimental system to specifically inhibit nuclear *de novo* NAD^+ synthesis (Fig. 2). The content of NAD^+ is known to differ between cellular compartments, such as the nucleus, cytoplasm, and mitochondria (3). However, the significance of NAD^+ compartmentalization has been unclear (3). This is because the role of NAD^+ homeostasis in cellular senescence has mostly been studied in terms of NAD^+ metabolism in the cytosol, where the majority of NAD^+ metabolism takes place. Here, using our established experimental system, we successfully revealed the role of nuclear *de novo* NAD^+ synthesis. We showed that NAD syn1, which is recruited to the sites of DNA damage via H2AX K5 Ac, is required for the PARylation activity of PARP-1 for H2AX dynamics. Importantly, the role of nuclear *de novo* NAD^+ synthesis is not restricted to the site of DNA damage. The inhibition of nuclear *de novo* NAD^+ synthesis alone was sufficient to disrupt whole-cell NAD^+ homeostasis and reduce mitochondrial energy metabolism, leading to the induction of premature cellular senescence (Fig. 4) and resulting in increased genome instability and accelerated anchorage independence of growth, which correlate closely with tumorigenicity (Fig. 5). Accordingly, the novel role of nuclear *de novo* NAD^+ synthesis, which is regulated by histone dynamics, is not only the control of local NAD^+-dependent enzymatic activity but also the regulation of whole-cell NAD^+ metabolism upon genome damage stress. Our study has elucidated a new aspect of NAD^+ compartmentalization and will lead to a more comprehensive understanding of how cells prevent cellular senescence and cancer by protecting against genome DNA damage.

Cellular senescence either autonomously suppresses tumorigenesis or nonautonomously promotes tumorigenesis in neighboring cells, via the secreting inflammatory senescence-associated secretory phenotype (SASP) (43–45). In this study, we found a novel NAD^+ synthesis-dependent aspect of cellular senescence, which induced genomic instability and promoted tumorigenesis when compromised. The compromised nuclear *de novo* NAD^+ synthesis may either autonomously or nonautonomously affect the whole-cell NAD^+ metabolism to induce genomic instability and promote tumorigenesis. For the latter case, the possible role of SASPs in this process should be investigated. The DNA repair capacity reportedly declines with age, and such genome instability could be a causal factor in age-related pathologies (1, 35). We propose that the nuclear *de novo* NAD^+ synthesis pathway, controlled by H2AX dynamics, is a mechanism to suppress the age-dependent decline of DNA repair capacity to prevent tumorigenesis. This function might be related to the regulation via cellular NAD^+ homeostasis and mitochondrial energy metabolism (1). Thus, focusing on nuclear *de novo* NAD^+ synthesis will be a novel approach for preventing age-related pathology.

FIG 5 Legend (Continued)

syn1-WT- or -G514E-expressing HepG2 cells. $n = 3$. Error bars show SD. HR activity is presented as in arbitrary units relative to mock-treated cells (data not included in the graph). (B) (i) Immunohistochemistry analysis using an antibody against RAD51, in cells expressing NLS-NAD syn1-WT or -G514E with or without 3 Gy of irradiation, followed by a 60-min recovery. Cell images are shown. (ii) Quantification of RAD51 foci per cells. WT IR(−), $n = 153$; WT IR(+), $n = 150$; G514E IR(−), $n = 176$; G514E IR(+), $n = 164$. Cells which do not have RAD51 foci were omitted from the graphs. *P* values were determined with Students' *t* test. See Materials and Methods for details. (C) (i) Soft-agar growth assay in the NLS-NAD syn1-WT (WT) or -G514E (G514E) expressing HepG2 cells with or without 3 Gy IR prior to the assay. (ii) Quantification of cell growth in the soft-agar growth assay from panel C. $n = 5$. Error bars show SD. *P* values were determined with Student's *t* test.

In various metabolic processes, such as purine biosynthesis, the *de novo* pathway consumes more amino acids than the salvage pathway, which has fewer reaction steps (46). The metabolic shift to the *de novo* pathway from the salvage pathway occurs to meet the increasing demand for metabolites, and this metabolic shift resembles several hallmarks of the metabolism in cancer cells, which require more amino acids such as glutamine for rapid proliferation (46). In this study, we used HepG2, a hepatocellular carcinoma cell line. In HepG2 cells, nuclear *de novo* NAD^+ synthesis, which consumes glutamine and tryptophan, might be used to maintain their proliferation capacity and thus avoid senescence and excess mutagenesis. Conversely, in noncancerous cells, nuclear *de novo* NAD^+ synthesis may be utilized to maintain optimum levels of NAD^+ to prevent metabolic maladaptation and tumorigenesis when cells encounter cellular stressors during the aging process. It will be important to use noncancerous cells, such as primary hepatocyte cells, for further understanding of how nuclear *de novo* NAD^+ synthesis contributes to the prevention of age-related pathologies.

PARP-1 is a repair protein for single-stranded DNA breaks, and recently, its function for DSBs has become clear (38). In this and previous studies, we showed that PARP-1, controlled via H2AX dynamics at DSB sites, is a critical regulator to activate nuclear *de novo* NAD^+ synthesis, which can prevent premature cellular senescence (12). So far, as NAD^+-consuming enzymes, sirtuins are regarded as longevity proteins, especially because of their role in the context of calorie restriction (1, 3, 34). In our view, PARP-1 can also be regarded as a longevity protein comparable to sirtuins in the context of DNA damage stress. Consistently, TIP60 is reportedly involved in controlling longevity in *Caenorhabditis elegans* (47). In this regard, PARP-1 will become an attractive target for preventing age-related pathologies by considering the regulation of chromatin dynamics.

We have shown that *de novo* NAD synthetase in the cell nucleus plays a pivotal role, not only in locally providing NAD^+ for the catalytic activity of PARP-1 for H2AX dynamics at sites of DNA damage, but also by providing NAD^+/NADH as cofactors to maintain mitochondrial energy metabolism. These two functions are coordinated via acetylation-dependent H2AX dynamics, to prevent senescence-associated genomic instability and tumorigenesis. Therefore, the nuclear *de novo* NAD^+ synthesis not only represents a new therapeutic target for age-related pathologies but also provides new insights for research fields focusing on cancer and neurodegenerative diseases.

MATERIALS AND METHODS

Antibodies. Immunoblotting analyses were performed with anti-TIP60 (kind gift from H. Hosokawa, Kyoto University), anti-acetylated H2AX (K5) (Millipore, AB10020), anti-NAD syn1 (Sigma), anti-glyceraldehyde-3-phosphate dehydrogenase (anti-GAPDH) (Gene Tex, GTX100118), anti-H2AX (Abcam, ab11175), M2 (anti-DYKDDDDK; Nacalai Tesque, NU01102), anti-RAD51 (Bioacademia, 70-012), γH2AX (mouse, Millipore, 05-636; rabbit, Millipore, 07-164), PARP-1 (Santa Cruz), PAR (Trevigen), GFP (Abcam, ab290), and anti-myc (MBL, 562) antibodies.

Cell culture and transfection. HeLa cells (kind gift from Y. Nakatani, Dana-Farber Cancer Institute) and HepG2 cells (JCRB1054) were cultured in Dulbecco's modified Eagle's medium (DMEM) supplemented with 10% newborn calf serum and 10% fetal bovine serum, respectively. For establishing stable HeLa or HepG2 cell lines expressing pOZ-eTIP60, pOZ-eTIPM, pOZ-eH2AX, or pOZ-eH2AXK5R, a retrovirus infection system was used as described previously. Stable HepG2 cell lines expressing TIP60, TIPM, H2AX, H2AXK5R, NLS-NAD syn1-WT, and NLS-NAD syn1-G514E under the control of the pCAGGS promoter were established by using the GeneJuice transfection reagent (Millipore) and selected with hygromycin.

siRNA. Human TIP60, H2AX, or PARP-1 27-mer siRNA was constructed by Integrated DNA Technologies (IDT). Target sequences were as follows: TIP60, 5′-GGACATCAGTGGCCGGAAGC-3′; H2AX, 5′-CTGGAATTCTGCA GCTAAC-3′; PARP-1, 5′-AAGGCTGGAGAGAGATTCTGTT-3′.

The siRNAs of NAD syn1 were purchased from Ambion. Target sequences were as follows: s30396 (siRNA NAD syn1-1), 5′-GGGTGGATCTCGTGACTAT-3′; s30395 (siRNA NAD syn1-2), 5′-CAGTTTCGGTGC ATAGAAA-3′. siRNAs were transfected by using RNAi Max reagent (Invitrogen).

Biochemistry. Affinity purifications of the H2AX complex and its regulatory complexes (acetyl-transferase TIP60 or UBC13) were performed as previously described. Protein sequences were determined by tandem mass spectrometry (MS/MS) using a Q-Tof Ultima API (Waters, Milford, MA, USA). Peptide peak picking was performed by Mascot Distiller, version 2.3 (Matrix Science, London, United Kingdom). Protein identification was done by a Mascot database search (version 2.3; Matrix Science) of all tandem mass spectra against the Human MS International Protein Index protein sequence database, version 3.53. Initially, NAD syn1 was identified as a component of the UBC13 complex. Since the UBC13 complex shares several protein components with the H2AX complex, we examined whether NAD syn1 is also

included in the protein complexes of H2AX. We performed immunoblot analysis using the antibody against NAD syn1 and confirmed NAD syn1 in these H2AX complexes.

Enzymatic assay for NAD syn1. Myc-tagged NLS-NAD syn1-WT or G514E was expressed in HepG2 cells and purified using a c-Myc-tagged mild purification kit (MBL) according to the manufacturer's instructions. Assays were based on the work of Wojcik et al. (26). The activities of NLS-NAD syn1-WT and -G514E were determined in reaction buffer composed of 2 mM ATP, 5 mM $MgCl_2$, 50 mM Tris-HCl (pH 8.0), 56 mM KCl, and 0.2 mg/mL bovine serum albumin. As substrates, 1 mM NAD and 20 mM glutamine were added. Two or six microliters of myc peptide-eluted enzymes was used for each reaction with incubation for 180 min at 37°C. Reactions were terminated in a boiling water bath, and the mixtures were heated for 3 min, followed by incubation on ice (3 min), and centrifuged for 10 min at 12,000 rpm. To quantify NAD^+, a NAD/NADH assay kit-WST (Dojindo) was used according to the manufacturer's instructions. For the comparison of the NAD^+ synthetase activity between the WT and the G514E mutant, the amount of NLS-NAD syn1-WT or -G514E per microliter of purified products was determined by Western blotting; then, a calibration curve was drawn from the quantification results to calculate the NAD^+ synthetase activity per amount of each purified protein.

Glutamine quantification. To measure the intracellular amounts of glutamate and glutamine, a glutamate assay kit-WST and a glutamine assay kit-WST (Dojindo) were used, respectively. HepG2 or HeLa cells irradiated at 2 Gy and then cultured for 0 min, 10 min, 60 min, or 120 min before the harvest of the cells. At each time point, 5×10^5 cells were harvested. Cells were collected via trypsinization and then washed with cold phosphate-buffered saline (PBS) (1 mL). The assays were performed according to the manufacturer's instructions.

Microirradiation and FRAP. FRAP analysis with microirradiation was performed using the 405-nm line of a UV laser (Leica). For the quantification of the fluorescence recovery, single optical sections for each time point were collected. The fluorescent intensities were quantified by Image J. The background fluorescence intensity (BG) and the average fluorescence intensity in the UV-microirradiated and bleached region at each time point (I_t) were quantified as previously described (16). For each time point, the relative intensity ($I_{rel;t}$) was calculated as $(I_t - BG)/(I_0 - BG)$, where I_0 is the average intensity of the region of interest (ROI) before the bleaching procedure. The percent recovery after each time point in the FRAP analysis ($P_{recovery;t}$) was calculated and normalized using the following formula: $100 \times (I_{rel;t})/(I_{norm;t})$, where $I_{norm;t}$ is the relative fluorescence intensity, calculated by the same method as $I_{rel;t}$, in the unbleached, UV-microirradiated region. Mean residence time was calculated using the curve-fitting application of MATLAB (27). The Wilcoxon rank sum test was used for statistical evaluation.

ChIP. Cells were transfected with Cas9-gRNA (AAVS1 region). Four hours after the transfection, cells were fixed with 1% formaldehyde for 10 min at room temperature before the addition of 125 mM glycine to stop cross-linking. The harvested cells were washed with fluorescence-activated cell sorting (FACS) buffer (PBS containing 2% newborn calf serum, 0.05% sodium azide, and 200 nM phenylmethylsulfonyl fluoride [PMSF]) at 4°C with rotation for 5 min. The cells were collected by centrifugation and resuspended in 250 μL SDS lysis buffer (50 mM Tris-HCl [pH 8.0], 10 mM EDTA, and 1% SDS). After incubation for 10 min at room temperature, the lysates were sonicated (Bioruptor; 5 times for 10 s; low power) and centrifuged; then, 1,800 μL of ChIP dilution buffer (50 mM Tris-HCl [pH 8.0], 167 mM NaCl, 1.1% Triton X-100, 0.11% sodium deoxycholate, and 200 nM PMSF) was added to 200 μL of the supernatant. The supernatant was further incubated with normal rabbit or mouse IgG (Santa Cruz) (4°C, 30 min with rotation) and then incubated with protein G agarose (Pierce, 20398) (4°C, 2 h with rotation) to preclear the samples. Five percent of each supernatant was used as the input control with the cross-linking reversal step. The rest of the supernatant (30% of the total) was incubated with magnetic beads (Pierce protein A/G magnetic beads, 88802) preconjugated with the anti-NAD syn1 antibody (overnight 4°C with rotation). The beads were washed sequentially with 1× radioimmunoprecipitation assay (RIPA)–150 mM NaCl (50 mM Tris-HCl [pH 8.0], 150 mM NaCl, 1 mM EDTA, 0.1% SDS, 1% Triton X-100, and 0.1% sodium deoxycholate), 1× RIPA–500 mM NaCl (50 mM Tris-HCl [pH 8.0], 500 mM NaCl, 1 mM EDTA, 0.1% SDS, 1% Triton X-100, and 0.1% sodium deoxycholate), and LiCl wash buffer (10 mM Tris-HCl [pH 8.0], 1 mM EDTA, 250 mM LiCl, 0.5% NP-40, 0.5% sodium deoxycholate) and twice with TE (10 mM Tris-HCl [pH 8.0], and 1 mM EDTA). After the washing with TE, cross-linking was reversed in 200 μL ChIP elution buffer (10 mM Tris-HCl [pH 8.0], 5 mM EDTA, 300 mM NaCl, 0.5% SDS) at 65°C for 7.5 h. Subsequently, RNase A (Sigma; 4 mg/mL, 37°C for 30 min) and proteinase K (Wako; 520 mg/mL, 5°C for 2.5 h) were added to the samples. The DNA was extracted with a ChIP DNA Clean & Concentrator kit (Zymo Research, D5201), according to the manufacturer's instructions (Active Motif). Each sample was analyzed by real-time PCR, using a Light Cycler 96 (Roche) and a KAPA SYBR Fast PCR kit. Cutting efficiency were determined by the $\Delta\Delta C_T$ method. Real-time PCR was performed using the following primers: AAVS-180 F, 5′-CCCGAATCCACAGGAGAACG-3′; AAVS-180 R, 5′-GACAACCCCAAAGTACCCCG-3′; AAVS-600 F, 5′-GTGCTCCGGAAAGAGCATCC-3′; AAVS-600 R, 5′-CCTTCAGGTTCCGTCTTCCTC-3′; AAVS-3100 F, 5′-TCTCAAGGCATGCTGGGATT-3′; and AAVS-3100 R, 5′-GCGGGATCCGTAAGGTGAAG-3′.

Assay for site-specific HR activity. The ASHRA was performed as previously described (39). A Cas9/gRNA expression vector for the ACTB locus, a Cas9/gRNA expression vector (Cas9-ACTB) for control transfection (scrambled gRNA [Cas9-scr]), and donor vector for the ACTB locus (pBS-ACTB-GFP-DV) were cotransfected using GeneJuice. Forty-eight hours after the transfection of Cas9 vectors, cells were harvested. The genomic DNA were collected using an RBC genomic DNA extraction kit (SciTrove). Each genomic DNA was analyzed by real-time PCR, using an Eco real-time PCR system (Illumina) and a KAPA SYBR Fast PCR kit. The relative quantity of the knock-in allele was applied by the $\Delta\Delta C_T$ method as described. Primer sequences are as follows: ACTB ref F2, AGTTGCGTTACACCCTTTCTTG; ACTB-common-

R1, GTGCAATCAAAGTCCTCGGC for the reference allele of *ACTB*; GFP-F3, CTGCCCGACAACCACTACCT; ACTB-common-R2, AGTCCTCGGCCACATTGTGAA for the fusion allele of *ACTB*.

Immunohistochemistry analysis. After the induction of IR, the cells were fixed with 4% paraformaldehyde (PFA) for 10 min. Anti-γ-H2AX (1:2,000) and RAD51 (1:5,000) antibodies in 1% bovine serum albumin–1× PBS were used. Cy3-conjugated AffiniPure donkey anti-mouse IgG (heavy plus light chain [H+L]) for γ-H2AX (Jackson ImmunoResearch, 715-165-151) and CF488A goat anti-rabbit IgG (H+L) for RAD51 (Biotium, 20019-1) were used as the secondary antibodies. Nuclei were stained with DAPI (4′,6-diamidino-2-phenylindole; Roche, 10 236 276 001). Samples were examined by immunofluorescence microscopy (Keyence, BZ-9000). To score foci, the hybrid-cell counting system (Keyence) was used.

JC-1 staining of mitochondria. The detection of mitochondrial energy metabolism was performed using a JC-1 MitoMP detection kit (Dojindo), following the manufacturer's instructions. Briefly, cells were stained with JC-1 and analyzed by fluorescence microscopy (BZ-9000; Keyence), and in parallel, cells were monitored by spectrophotometry analysis using an ARVO-X spectrophotometer (Perkin Elmer). For monitoring the monomeric JC-1 signal, an excitation filter at 485 nm and an emission filter at 535 nm were used (0.1s). For monitoring aggregated JC-1 signal, an excitation filter at 531 nm/25 nm and an emission filter at 590 nm/10 nm were used (0.1s).

Analysis of cellular senescence. *In situ* staining of SA-β-Gal was performed using a senescence detection kit (Abcam, ab65351). For the quantification of SA-β-Gal, a cellular senescence detection kit, SPiDER-β-Gal (Dojindo, SG05), was used according to the manufacturer's instructions. The SPiDER-β-Gal signal was quantified using an ARVO-X spectrophotometer with a 531-nm excitation filter and a 581-nm emission filter. The value was divided by the value from a blank well. The fold increases of SA-β-Gal compared to the blank signal are presented as arbitrary units of SA-β-Gal activity.

Soft-agar colony formation assay and collagen gel culture. A soft-agar colony formation assay was performed with the Cytoselect 96-well cell transformation assay kit (CBA-130; Cell Biolabs, Inc., San Diego, CA, USA) in accordance with the manufacturer's instructions. Briefly, cells were suspended in DMEM containing 10% fetal bovine serum with 0.4% agarose and layered on the bottom agar layer in each well of 96-well plates. Cultures were maintained for 7 days at 37°C and 5% CO_2. Data were obtained from three independent experiments. The cell number was quantified with CyQuant GR dye (included in the kit) in a fluorescence plate reader using a 520-nm filter (emission, 485 nm) using an ARVO-X spectrophotometer. For collagen gel culture, AteloCell IPC-50 atelocollagen was used, following the manufacture's instructions (Koken). Giemsa staining was performed after methanol fixation.

SUPPLEMENTAL MATERIAL

Supplemental material is available online only.

SUPPLEMENTAL FILE 1, PDF file, 2.8 MB.

ACKNOWLEDGMENTS

We thank Takuma Shiraki for critical comments and helpful suggestions. This work was supported by Grant-in-Aid for Scientific Research (B: 20H04336), a grant from Suzuken Memorial Foundation to T.I. Grant-in-Aid for Scientific Research (C: 19K12321), to M.I. This work was also partly supported by the Cooperative Research Project Program at the IDAC, Tohoku University, and "Strategic Research Projects" grant from ROIS to K.F.

REFERENCES

1. Demarest TG, Babbar M, Okur MN, Dan X, Croteau DL, Fakouri NB, Mattson MP, Bohr VA. 2019. NAD+ metabolism in aging and cancer. Annu Rev Cancer Biol 3:105–130. https://doi.org/10.1146/annurev-cancerbio-030518-055905.
2. Xie N, Zhang L, Gao W, Huang C, Huber PE, Zhou X, Li C, Shen G, Zou B. 2020. NAD(+) metabolism: pathophysiologic mechanisms and therapeutic potential. Signal Transduct Target Ther 5:227. https://doi.org/10.1038/s41392-020-00311-7.
3. Canto C, Menzies KJ, Auwerx J. 2015. NAD(+) metabolism and the control of energy homeostasis: a balancing act between mitochondria and the nucleus. Cell Metab 22:31–53. https://doi.org/10.1016/j.cmet.2015.05.023.
4. Yaku K, Okabe K, Nakagawa T. 2018. NAD metabolism: implications in aging and longevity. Ageing Res Rev 47:1–17. https://doi.org/10.1016/j.arr.2018.05.006.
5. Shi H, Enriquez A, Rapadas M, Martin E, Wang R, Moreau J, Lim CK, Szot JO, Ip E, Hughes JN, Sugimoto K, Humphreys DT, McInerney-Leo AM, Leo PJ, Maghzal GJ, Halliday J, Smith J, Colley A, Mark PR, Collins F, Sillence DO, Winlaw DS, Ho JWK, Guillemin GJ, Brown MA, Kikuchi K, Thomas PQ, Stocker R, Giannoulatou E, Chapman G, Duncan EL, Sparrow DB, Dunwoodie SL. 2017. NAD deficiency, congenital malformations, and niacin supplementation. N Engl J Med 377:544–552. https://doi.org/10.1056/NEJMoa1616361.
6. Liu L, Su X, Quinn WJ, III, Hui S, Krukenberg K, Frederick DW, Redpath P, Zhan L, Chellappa K, White E, Migaud M, Mitchison TJ, Baur JA, Rabinowitz JD. 2018. Quantitative analysis of NAD synthesis-breakdown fluxes. Cell Metab 27:1067–1080.E5. https://doi.org/10.1016/j.cmet.2018.03.018.
7. Poyan Mehr A, Tran MT, Ralto KM, Leaf DE, Washco V, Messmer J, Lerner A, Kher A, Kim SH, Khoury CC, Herzig SJ, Trovato ME, Simon-Tillaux N, Lynch MR, Thadhani RI, Clish CB, Khabbaz KR, Rhee EP, Waikar SS, Berg AH, Parikh SM. 2018. De novo NAD(+) biosynthetic impairment in acute kidney injury in humans. Nat Med 24:1351–1359. https://doi.org/10.1038/s41591-018-0138-z.
8. Katsyuba E, Mottis A, Zietak M, De Franco F, van der Velpen V, Gariani K, Ryu D, Cialabrini L, Matilainen O, Liscio P, Giacche N, Stokar-Regenscheit N, Legouis D, de Seigneux S, Ivanisevic J, Raffaelli N, Schoonjans K, Pellicciari R, Auwerx J. 2018. De novo NAD(+) synthesis enhances mitochondrial function and improves health. Nature 563:354–359. https://doi.org/10.1038/s41586-018-0645-6.
9. Tummala KS, Gomes AL, Yilmaz M, Grana O, Bakiri L, Ruppen I, Ximenez-Embun P, Sheshappanavar V, Rodriguez-Justo M, Pisano DG, Wagner EF, Djouder N. 2014. Inhibition of de novo NAD(+) synthesis by oncogenic URI causes liver tumorigenesis through DNA damage. Cancer Cell 26:826–839. https://doi.org/10.1016/j.ccell.2014.10.002.
10. Fjeld CC, Birdsong WT, Goodman RH. 2003. Differential binding of NAD+ and NADH allows the transcriptional corepressor carboxyl-terminal binding protein to serve as a metabolic sensor. Proc Natl Acad Sci U S A 100:9202–9207. https://doi.org/10.1073/pnas.1633591100.

11. Katoh Y, Ikura T, Hoshikawa Y, Tashiro S, Ito T, Ohta M, Kera Y, Noda T, Igarashi K. 2011. Methionine adenosyltransferase II serves as a transcriptional corepressor of Maf oncoprotein. Mol Cell 41:554–566. https://doi.org/10.1016/j.molcel.2011.02.018.
12. Ikura M, Furuya K, Fukuto A, Matsuda R, Adachi J, Matsuda T, Kakizuka A, Ikura T. 2016. Coordinated regulation of TIP60 and poly(ADP-ribose) polymerase 1 in damaged-chromatin dynamics. Mol Cell Biol 36:1595–1607. https://doi.org/10.1128/MCB.01085-15.
13. Zhang T, Berrocal JG, Frizzell KM, Gamble MJ, DuMond ME, Krishnakumar R, Yang T, Sauve AA, Kraus WL. 2009. Enzymes in the NAD+ salvage pathway regulate SIRT1 activity at target gene promoters. J Biol Chem 284:20408–20417. https://doi.org/10.1074/jbc.M109.016469.
14. Zhang T, Berrocal JG, Yao J, DuMond ME, Krishnakumar R, Ruhl DD, Ryu KW, Gamble MJ, Kraus WL. 2012. Regulation of poly(ADP-ribose) polymerase-1-dependent gene expression through promoter-directed recruitment of a nuclear NAD+ synthase. J Biol Chem 287:12405–12416. https://doi.org/10.1074/jbc.M111.304469.
15. Ikura T, Ogryzko VV, Grigoriev M, Groisman R, Wang J, Horikoshi M, Scully R, Qin J, Nakatani Y. 2000. Involvement of the TIP60 histone acetylase complex in DNA repair and apoptosis. Cell 102:463–473. https://doi.org/10.1016/s0092-8674(00)00051-9.
16. Ikura T, Tashiro S, Kakino A, Shima H, Jacob N, Amunugama R, Yoder K, Izumi S, Kuraoka I, Tanaka K, Kimura H, Ikura M, Nishikubo S, Ito T, Muto A, Miyagawa K, Takeda S, Fishel R, Igarashi K, Kamiya K. 2007. DNA damage-dependent acetylation and ubiquitination of H2AX enhances chromatin dynamics. Mol Cell Biol 27:7028–7040. https://doi.org/10.1128/MCB.00579-07.
17. Ikura M, Furuya K, Matsuda S, Matsuda R, Shima H, Adachi J, Matsuda T, Shiraki T, Ikura T. 2015. Acetylation of histone H2AX at Lys 5 by the TIP60 histone acetyltransferase complex is essential for the dynamic binding of NBS1 to damaged chromatin. Mol Cell Biol 35:4147–4157. https://doi.org/10.1128/MCB.00757-15.
18. Bogan KL, Brenner C. 2008. Nicotinic acid, nicotinamide, and nicotinamide riboside: a molecular evaluation of NAD+ precursor vitamins in human nutrition. Annu Rev Nutr 28:115–130. https://doi.org/10.1146/annurev.nutr.28.061807.155443.
19. Hu L, Ibrahim K, Stucki M, Frapolli M, Shahbeck N, Chaudhry FA, Gorg B, Haussinger D, Penberthy WT, Ben-Omran T, Haberle J. 2015. Secondary NAD+ deficiency in the inherited defect of glutamine synthetase. J Inherit Metab Dis 38:1075–1083. https://doi.org/10.1007/s10545-015-9846-4.
20. Matsuda S, Adachi J, Ihara M, Tanuma N, Shima H, Kakizuka A, Ikura M, Ikura T, Matsuda T. 2016. Nuclear pyruvate kinase M2 complex serves as a transcriptional coactivator of arylhydrocarbon receptor. Nucleic Acids Res 44:636–647. https://doi.org/10.1093/nar/gkv967.
21. Tang J, Cho NW, Cui G, Manion EM, Shanbhag NM, Botuyan MV, Mer G, Greenberg RA. 2013. Acetylation limits 53BP1 association with damaged chromatin to promote homologous recombination. Nat Struct Mol Biol 20:317–325. https://doi.org/10.1038/nsmb.2499.
22. Aymard F, Bugler B, Schmidt CK, Guillou E, Caron P, Briois S, Iacovoni JS, Daburon V, Miller KM, Jackson SP, Legube G. 2014. Transcriptionally active chromatin recruits homologous recombination at DNA double-strand breaks. Nat Struct Mol Biol 21:366–374. https://doi.org/10.1038/nsmb.2796.
23. Zheng D, Ezzeddine N, Chen CY, Zhu W, He X, Shyu AB. 2008. Deadenylation is prerequisite for P-body formation and mRNA decay in mammalian cells. J Cell Biol 182:89–101. https://doi.org/10.1083/jcb.200801196.
24. Suda Y, Tachikawa H, Yokota A, Nakanishi H, Yamashita N, Miura Y, Takahashi N. 2003. Saccharomyces cerevisiae QNS1 codes for NAD(+) synthetase that is functionally conserved in mammals. Yeast 20:995–1005. https://doi.org/10.1002/yea.1008.
25. Kalderon D, Roberts BL, Richardson WD, Smith AE. 1984. A short amino acid sequence able to specify nuclear location. Cell 39:499–509. https://doi.org/10.1016/0092-8674(84)90457-4.
26. Wojcik M, Seidle HF, Bieganowski P, Brenner C. 2006. Glutamine-dependent NAD+ synthetase. How a two-domain, three-substrate enzyme avoids waste. J Biol Chem 281:33395–33402. https://doi.org/10.1074/jbc.M607111200.
27. Lukas C, Melander F, Stucki M, Falck J, Bekker-Jensen S, Goldberg M, Lerenthal Y, Jackson SP, Bartek J, Lukas J. 2004. Mdc1 couples DNA double-strand break recognition by Nbs1 with its H2AX-dependent chromatin retention. EMBO J 23:2674–2683. https://doi.org/10.1038/sj.emboj.7600269.
28. Zahradka P, Ebisuzaki K. 1982. A shuttle mechanism for DNA-protein interactions. The regulation of poly(ADP-ribose) polymerase. Eur J Biochem 127:579–585.
29. Ferro AM, Olivera BM. 1982. Poly(ADP-ribosylation) in vitro. Reaction parameters and enzyme mechanism. J Biol Chem 257:7808–7813. https://doi.org/10.1016/S0021-9258(18)34453-3.
30. Langelier MF, Pascal JM. 2013. PARP-1 mechanism for coupling DNA damage detection to poly(ADP-ribose) synthesis. Curr Opin Struct Biol 23:134–143. https://doi.org/10.1016/j.sbi.2013.01.003.
31. He J, Hu B, Shi X, Weidert ER, Lu P, Xu M, Huang M, Kelley EE, Xie W. 2013. Activation of the aryl hydrocarbon receptor sensitizes mice to nonalcoholic steatohepatitis by deactivating mitochondrial sirtuin deacetylase Sirt3. Mol Cell Biol 33:2047–2055. https://doi.org/10.1128/MCB.01658-12.
32. Stein LR, Imai S. 2012. The dynamic regulation of NAD metabolism in mitochondria. Trends Endocrinol Metab 23:420–428. https://doi.org/10.1016/j.tem.2012.06.005.
33. Smiley ST, Reers M, Mottola-Hartshorn C, Lin M, Chen A, Smith TW, Steele GD, Jr, Chen LB. 1991. Intracellular heterogeneity in mitochondrial membrane potentials revealed by a J-aggregate-forming lipophilic cation JC-1. Proc Natl Acad Sci U S A 88:3671–3675. https://doi.org/10.1073/pnas.88.9.3671.
34. Wiley CD, Campisi J. 2021. The metabolic roots of senescence: mechanisms and opportunities for intervention. Nat Metab 3:1290–1301. https://doi.org/10.1038/s42255-021-00483-8.
35. Petr MA, Tulika T, Carmona-Marin LM, Scheibye-Knudsen M. 2020. Protecting the aging genome. Trends Cell Biol 30:117–132. https://doi.org/10.1016/j.tcb.2019.12.001.
36. Krenning L, van den Berg J, Medema RH. 2019. Life or death after a break: what determines the choice? Mol Cell 76:346–358. https://doi.org/10.1016/j.molcel.2019.08.023.
37. Caron MC, Sharma AK, O'Sullivan J, Myler LR, Ferreira MT, Rodrigue A, Coulombe Y, Ethier C, Gagne JP, Langelier MF, Pascal JM, Finkelstein IJ, Hendzel MJ, Poirier GG, Masson JY. 2019. Poly(ADP-ribose) polymerase-1 antagonizes DNA resection at double-strand breaks. Nat Commun 10:2954. https://doi.org/10.1038/s41467-019-10741-9.
38. Helleday T, Bryant HE, Schultz N. 2005. Poly(ADP-ribose) polymerase (PARP-1) in homologous recombination and as a target for cancer therapy. Cell Cycle 4:1176–1178. https://doi.org/10.4161/cc.4.9.2031.
39. Yoshino Y, Endo S, Chen Z, Qi H, Watanabe G, Chiba N. 2019. Evaluation of site-specific homologous recombination activity of BRCA1 by direct quantitation of gene editing efficiency. Sci Rep 9:1644. https://doi.org/10.1038/s41598-018-38311-x.
40. Helleday T. 2010. Homologous recombination in cancer development, treatment and development of drug resistance. Carcinogenesis 31:955–960. https://doi.org/10.1093/carcin/bgq064.
41. Carr AM, Lambert S. 2013. Replication stress-induced genome instability: the dark side of replication maintenance by homologous recombination. J Mol Biol 425:4733–4744. https://doi.org/10.1016/j.jmb.2013.04.023.
42. Cifone MA, Fidler IJ. 1980. Correlation of patterns of anchorage-independent growth with in vivo behavior of cells from a murine fibrosarcoma. Proc Natl Acad Sci U S A 77:1039–1043. https://doi.org/10.1073/pnas.77.2.1039.
43. Chan ASL, Narita M. 2019. Short-term gain, long-term pain: the senescence life cycle and cancer. Genes Dev 33:127–143. https://doi.org/10.1101/gad.320937.118.
44. Acosta JC, O'Loghlen A, Banito A, Guijarro MV, Augert A, Raguz S, Fumagalli M, Da Costa M, Brown C, Popov N, Takatsu Y, Melamed J, d'Adda di Fagagna F, Bernard D, Hernando E, Gil J. 2008. Chemokine signaling via the CXCR2 receptor reinforces senescence. Cell 133:1006–1018. https://doi.org/10.1016/j.cell.2008.03.038.
45. Kuilman T, Michaloglou C, Vredeveld LC, Douma S, van Doorn R, Desmet CJ, Aarden LA, Mooi WJ, Peeper DS. 2008. Oncogene-induced senescence relayed by an interleukin-dependent inflammatory network. Cell 133:1019–1031. https://doi.org/10.1016/j.cell.2008.03.039.
46. Huang Z, Xie N, Illes P, Di Virgilio F, Ulrich H, Semyanov A, Verkhratsky A, Sperlagh B, Yu SG, Huang C, Tang Y. 2021. From purines to purinergic signalling: molecular functions and human diseases. Signal Transduct Target Ther 6:162. https://doi.org/10.1038/s41392-021-00553-z.
47. Ikeda T, Uno M, Honjoh S, Nishida E. 2017. The MYST family histone acetyltransferase complex regulates stress resistance and longevity through transcriptional control of DAF-16/FOXO transcription factors. EMBO Rep 18:1716–1726. https://doi.org/10.15252/embr.201743907.